NASA TECHNICAL MEMORANDUM

NASA TM X-1517

NASA TM X-1517

EFFECT OF BOATTAIL JUNCTURE SHAPE ON PRESSURE DRAG COEFFICIENTS OF ISOLATED AFTERBODIES

by George D. Shrewsbury

Lewis Research Center

Cleveland, Ohio

NATIONAL AERONAUTICS AND SPACE ADMINISTRATION • WASHINGTON, D. C. • MARCH 1968

NASA TM X-1517

EFFECT OF BOATTAIL JUNCTURE SHAPE ON PRESSURE DRAG COEFFICIENTS OF ISOLATED AFTERBODIES

By George D. Shrewsbury

Lewis Research Center
Cleveland, Ohio

NATIONAL AERONAUTICS AND SPACE ADMINISTRATION

For sale by the Clearinghouse for Federal Scientific and Technical Information
Springfield, Virginia 22151 – CFSTI price $3.00

EFFECT OF BOATTAIL JUNCTURE SHAPE ON PRESSURE DRAG COEFFICIENTS OF ISOLATED AFTERBODIES

by George D. Shrewsbury

Lewis Research Center

SUMMARY

A variety of afterbodies were tested on a sting-supported model of a closed-inlet nacelle. Jet effects were simulated with a cylinder positioned downstream of the afterbody base. Axial-force coefficients were obtained for a 7° conical boattail and various 15° boattailed afterbodies on which the boattail juncture with the cylindrical portion of the nacelle had been smoothed with different radii of curvature. Data were obtained over a Mach number range of 0.56 to 1.00 at angles of attack from 0 to 8°.

The results indicate that increasing the boattail radius of curvature generally delays the occurrence of the transonic drag rise. With the 15° boattails, the sharp edge ($R/D_M = 0$) configuration had a drag-rise Mach number near 0.6. Increasing the radius of curvature to $R/D_M = 1$ delayed the drag-rise Mach number to approximately 0.8. For R/D_M of 2.5 or greater, the drag-rise Mach number occurred slightly above Mach 0.9.

INTRODUCTION

Supersonic airbreathing propulsion systems designed for Mach numbers up to 3.0 operate over a range of nozzle pressure ratios from approximately 2.0 to 30.0. Efficient performance of the propulsion system at all flight speeds requires variations in the nozzle expansion ratio. If the configuration utilizes nacelle-mounted engines and divergent ejector nozzles, it may have a nearly cylindrical afterbody at the design Mach number. Because of the high nozzle pressure ratio at the design Mach number, external flow effects have little effect on nozzle performance. Off-design operation, however, requires a boattailed afterbody of the engine nacelle in order to provide this decrease in expansion ratio. The drag incurred by boattailing the nacelle afterbody can be a significant portion of propulsion system net thrust, especially at subsonic cruise where the engine is throttled. Many supersonic aircraft missions may require that sizeable portions of the flight

be conducted at subsonic Mach numbers. The subsonic cruise Mach number selection is influenced by the boattail transonic drag rise characteristics. If the transonic drag rise can be delayed, a higher subsonic cruise Mach number may be permissible. Consequently, the drag characteristics of the nacelle afterbody become of significant importance at subsonic and transonic Mach numbers.

It has been demonstrated that circular arc afterbodies result in lower drag coefficients than conical afterbodies for equal boattail angles and ratios of base diameter to maximum diameter (ref. 1). Since most supersonic aircraft nozzle system geometries are variable, the full circular arc afterbody, although desirable from a drag viewpoint, is mechanically difficult to transform into a smooth cylinder for design Mach number operation. Therefore, it became desirable to investigate intermediate transition radii of curvature at subsonic and transonic Mach numbers.

An investigation was conducted in the Lewis 8- by 6-foot Supersonic Wind Tunnel to study the effect of varying the boattail transition radius of curvature on a 15° boattail with a ratio of base diameter to maximum diameter of 0.67. The jet was simulated with a solid cylinder which had a diameter equal to the afterbody base diameter. Four-inch diameter models were tested with six radii of curvature ranging from 0 (sharp corner) to $4.84\ D_M$ (tangent ogive). A 7° conical boattail with a L/D_M the same as the 15° conical boattail was also investigated. Data were obtained over a Mach number range of 0.56 to 1.00. The models were tested at angles of attack ranging from 0 to 8°. The test section Reynolds number ranged from 3.6×10^6 per foot to 4.6×10^6 per foot.

SYMBOLS

A	area
C_a	axial-force coefficient, axial force/$q_o A_M$
C_p	pressure coefficient $(p - p_o)/q_o$
D	diameter
L	model length from afterbody base
M	Mach number
p	static pressure
q	dynamic pressure
R	boattail juncture radius of curvature
V	velocity
X	axial distance aft of model afterbody interface

Y radial distance from model surface

α model angle of attack, deg

β boattail trailing-edge angle, deg

δ boundary layer thickness

Subscripts:

a axial

b afterbody base

e nozzle exit conditions

L local

M maximum

o free-stream conditions

s sting

β boattail surface

APPARATUS AND PROCEDURE

The complete afterbody model configurations, as installed in the Lewis 8- by 6-foot Supersonic Wind Tunnel, is shown in figure 1. The basic model was a sting-supported 4-inch-diameter (10.16 cm) cylindrical section with a 10^0 half-angle conical forebody. The length of this cylindrical section was varied to evaluate the effect of boundary layer thickness ahead of the afterbody region. Figure 2 is a sketch of the model installation showing the location of the short and long models in the perforated test section. The location of the forebody remained fixed, and the position of the afterbody moved aft when the model length was changed from short to long model configurations. The model length from the forebody shoulder to the model-afterbody interface varied from 5.91 to 10.91 model diameters.

Although reference 2 indicates the desirability of variable tunnel wall porosity with Mach number to minimize tunnel wall interference effects, a constant value of 3.1 percent was selected for this study. Other unpublished data from the 8 by 6 tunnel indicate that this is an acceptable compromise with 4-inch (10.16 cm) diameter models. Model blockage was 0.18 percent at a 0^o angle of attack.

The cylindrical portion of both model lengths was pressure instrumented at 2-inch (5.08 cm) intervals along the top and side. A boundary layer rake was installed on both model lengths to survey the local flow field ahead of the afterbody region and to measure

boundary layer thickness. The boundary layer survey plane was located 1 inch (2.54 cm) forward of the model-afterbody interface. The total pressures from the rake were used with static pressures located at 90° and 180° from the rake to compute values of V/V_o using the Rayleigh-pitot equation. Details of the boundary layer rake are shown in figure 3.

The afterbody geometries investigated are shown in figure 4. The afterbody geometries included a cylindrical afterbody, a 7° conical boattail, and 15° boattails with radii of curvature of 0 (sharp edge), 0.5, 1.0, 2.5, 3.5, and 4.84 model diameters. Details of the afterbody geometries are shown in figure 5. The cylindrical afterbody was a heavily instrumented extension of the cylindrical portion of the model. It was investigated to determine the static-pressure environment of the afterbody region as influenced by terminal shock waves from the conical forebody, wall reflected expansion and shock waves, and wall-generated disturbances. The 7° conical boattail was investigated to evaluate boattail angle effects. The boattail L/D_M of the 7° afterbody was the same as the 15° conical boattail. All 15° boattails had a ratio of base diameter to maximum diameter of 0.67. On boattails with radii of curvature, the curvature was tangent to the cylindrical portion of the afterbody. Since the ratio of base diameter to model diameter was held constant, increasing the radius of curvature increased the length of the boattail. The 4.84 R/D_M boattail is a tangent ogive configuration with the entire boattail being a curved surface.

Since the boattail axial-force coefficients were determined from boattail pressure measurements, extensive pressure instrumentation was located on the afterbodies. Instrumentation details for the 15° conical boattail are shown in figure 6. Instrumentation of all afterbody configurations was similar. The axial projection of the boattail was divided into 10 equal annular areas. Pressure taps were located around 180° of the centroid line of each annular area at 30° intervals. It was assumed that the local flow field would be symmetrical about a vertical plane through the model axis, so pressures were located only on one side of the boattail. Extra pressure taps were located near the corner of the boattails to help define boattail pressure distribution. These pressures were not used for drag determination.

By instrumenting the boattail in this manner, an area weighted average of pressure coefficient can be computed. This average pressure coefficient is then used to compute the axial-force coefficient. The boattail axial-force coefficient computed in this manner does not include the afterbody base drag or afterbody skin friction drag, but pertains only to those pressure forces acting on the boattail surface.

The afterbodies were tested in the presence of a cylindrical section extending from the afterbody base. The purpose of the cylinders was to approximate the local flow field that would exist if a jet were present with a value of $p_e/p_L = 1.0$. The simulator diameters were equal to the afterbody base diameters. Details of the jet simulators for the

7^{o} and 15^{o} boattails are shown in figure 7. The afterbodies were also tested with only the 1.62-inch (4.115 cm) support sting present to evaluate the effect of the jet simulator.

RESULTS AND DISCUSSION

Jet Simulator and Sting Effects

The experimental and calculated effects of different sting diameters on the drag of the 4.84 R/D_M (ogive) boattail are shown in figure 8. The boattail axial-force coefficients for the ogive boattail were corrected for sting effects by using the method developed in reference 3. The ogive boattail was used because the corrections made using this method are valid only for circular arc boattails, parabolic boattils, or conical boattails with angles less than 8^{o}. In addition, the corrections are valid only for Mach numbers below the transonic drag rise. By utilizing this method, the experimental data taken with the 1.62-inch (4.115 cm) sting were used to calculate the no-sting axial-force coefficients. The no-sting results were then adjusted for the jet simulator effect (by the same method), and a comparison with the experimental data was reasonably good as indicated by figure 8.

Boattail axial-force coefficients for the 15^{o} conical boattail are shown in figure 9 for the entire Mach number range. Data are shown with and without the jet simulator. The presence of the jet simulator results in a decrease in boattail axial-force coefficient for all Mach numbers investigated.

The effect of jet simulator on afterbody pressure distribution is shown for a 15^{o} conical boattail in figure 10. The presence of the jet simulator creates a stronger recompression region at the boattail trailing edge than exists with only the support sting present. At subsonic speeds the stronger recompression region causes higher pressures to propagate forward on the boattail surface. This effect was not as apparent at Mach 1.0.

A comparison of jet simulator data and cold jet data from reference 4 is shown in figure 11. The axial-force coefficients for the cold flow model are for a slightly different configuration in that $D_b/D_M = 0.65$. The cold jet data shown were interpolated values for $p_e/p_o = 1.0$. Since the local pressure at the base plane is nearly equal to free-stream static, a p_e/p_o of 1.0 should result in a nearly cylindrical jet. In general, the data are in good agreement except at Mach 1.0, which indicates that the effects of afterbody shape on drag-rise Mach number are valid utilizing this solid jet simulation technique.

Pressure Environments of Short and Long Model Configurations

The cylindrical afterbody was tested with both short and long model configurations to determine the presence of terminal shocks, reflected expansion and shock waves, and

wall-generated disturbances. The effect of afterbody location on cylindrical afterbody model pressure distributions is shown in figure 12. For the subsonic Mach numbers, the afterbodies of the short and long models are in nearly identical pressure environments. At Mach values of 0.67, 0.74, and 0.80, the local static pressures on both model lengths were slightly below free-stream pressure. This resulted in an increase in Mach number of approximately 0.01. At transonic Mach numbers, over-expansion at the shoulder of the forebody is severe enough that recompression along the cylindrical portion of the model is partially accomplished by a normal shock wave called a terminal shock. At Mach 1.0, the terminal shock wave is located approximately 4.0 model diameters forward of the afterbody base of the short model. The terminal shock wave occuring on the long model is located farther upstream from the afterbody region and is not seen in figure 12. The influence of terminal shock on afterbody pressures is small for both long and short models. With the cylindrical afterbody configuration, an inadvertent 0.003-inch (0.0076 cm) forward facing step existed at the model-afterbody interface. Disturbances from this step apparently created small pressure increases at Mach 1.00 approximately 1.5 model diameters forward of the afterbody base. Since this disturbance existed on both the long and short models, it could not have been a result of tunnel wall effects. This disturbance probably had little effect on the pressures in the afterbody region however, since the ratio of step height to model diameter is relatively small. Similar surface irregularities did not exist on the other afterbody configurations.

Boundary Layer

Boundary layer profiles for both short and long model configuration are shown in figure 13. The experimental data are compared with a theoretical seventh-power boundary layer profile. Both short and long model configurations have well developed turbulent profiles at all Mach numbers investigated. Boundary layer thicknesses for short and long model configurations are shown in figure 14 for all Mach numbers investigated. In general, the long model boundary layer is approximately 50 percent thicker than the short model boundary layer. At Mach 0.9, values of δ/D_M were 0.12 for the short model and 0.17 for the long model configurations. For reference purposes, a full-scale wing-mounted nacelle would typically have a δ/D_M value of approximately 0.05, and a fuselage installed afterbody would have a typical δ/D_M value of approximately 0.16.

The effect of boundary layer thickness on boattail axial-force coefficient is shown on figure 15. Data are shown for a 15^o sharp edge conical boattail without jet simulator for short and long model lengths. The short model afterbody has a higher axial-force coefficient over the entire Mach number range. For all Mach numbers, the decrement in axial-force coefficient is due to differences in boundary layer thickness only, since the afterbodies are in the same pressure environments. At Mach 0.9, increasing δ/D_M from 0.12 to 0.17 reduces the boattail axial-force coefficient approximately 12 percent.

In general, a greater boundary layer thickness results in a significant decrease in the axial-force coefficient of a 15° conical boattail with a sharp edge. Previous investigations (refs. 5 and 6) report negligible effects of boundary layer thickness on afterbody drag over the same range of boundary layer thickness ratios δ/D_M as this test.

The effect of boundary layer thickness on boattail pressure distribution at a representative Mach number of 0.9 is shown in figure 16. The presence of the thicker boundary layer causes a higher pressure to exist along the entire surface of the boattail.

Effect of Boattail Shape

The effect of afterbody shape on the transonic drag rise is shown in figure 17 for all 15° configurations and the 7° boattail. These and all subsequent data are shown for the short model configuration only. In general, increasing the value of R/D_M delays the occurrence of the transonic drag rise. The sharp edge ($R/D_M = 0$) boattail is already into the transonic drag rise at Mach 0.56. The 0.5 R/D_M and 1.0 R/D_M boattails have transonic drag rises that begin at approximately Mach 0.8. The transonic drag rise for the 2.5, 3.5, and 4.84 R/D_M boattails and the 7° boattail is delayed to slightly greater than Mach 0.9.

The effect of R/D_M on 15° boattail axial-force coefficients is shown in figure 18. The greatest reduction in axial-force coefficient obtained was 88 percent for an R/D_M of 3.5 at Mach 0.9. At Mach 0.8, smoothing the boattail juncture with an R/D_M of 0.50 reduced the axial-force coefficient 44 percent; at Mach 0.9, the same configuration reduced the axial-force coefficient by 27 percent. At the subsonic Mach numbers, increasing R/D_M above 3.5 had little or no effect on boattail axial-force coefficient. At Mach 1.0, however, the axial-force coefficient continues to decrease over the entire range of R/D_M investigated.

The effect of afterbody shape on the 15° afterbody pressure distributions is shown in figure 19. Data are also shown for the 7° boattail. At Mach 0.56, 0.7, and 0.8, increasing R/D_M decreases the overexpansion occurring on the 15° boattail surfaces. At Mach 0.9 and 1.0, increasing R/D_M has no significant effect on overexpansion except for R/D_M larger than 1.0. At Mach 0.7, the local velocity at the 15° sharp edge boattail corner has already reached sonic conditions. At Mach 1.0, the local Mach number on the 15° sharp edge boattail has reached approximately 1.60. At the subsonic free-stream Mach numbers, the recompression to subsonic Mach numbers along the boattail surface is accomplished smoothly by isentropic compression. At a free-stream Mach number of 1.0, however, the local Mach numbers are high enough that recompression is partially accomplished by a trailing oblique shock wave just downstream of the corner region on the 15° boattails with small values of R/D_M and the 7° boattail. The

presence of the oblique shock wave on the 15^{o} sharp edge boattail is verified by schlieren photographs of a similar boattail geometry shown in figure 5(b) of reference 1. In general, increasing R/D_M increases the value to which the pressure recovers at the aft end of the boattail.

Effect of Angle of Attack

The effect of angle of attack on the boattail transonic drag rise characteristics is shown in figure 20 for all configurations tested. For the 15^{o} boattails, angles of attack greater than 4^{o} caused increased boattail drag, but there was little apparent effect on drag-rise Mach number. For the 7^{o} conical boattail, the transonic drag rise begins at lower Mach numbers when the boattail is at angles of attack of 4^{o} or more. These results for the 15^{o} boattails are replotted as a function of angle of attack in figure 21. It is apparent that there was increased sensitivity to angle of attack as the juncture radius decreased at Mach numbers 0.8 and 0.9, but this effect was not as apparent at the other Mach numbers.

Pressure distributions of a 15^{o} sharp-edge boattil for different angles of attack are shown in figure 22. Data are presented for top, side, and bottom rows of instrumentation only for Mach 0.9, since circumferential trends in pressure distributions obtained at this Mach number were representative of those obtained at all Mach numbers. When the boattail is at an angle of attack, the higher pressures occur on the leeward side of the afterbody. This effect results in a destabilizing negative normal force. The trends in circumferential pressure distribution are in agreement with those presented in reference 7.

SUMMARY OF RESULTS

A variety of afterbodies were tested on a sting-supported model of a closed inlet nacelle. Jet effects were simulated with a cylinder positioned downstream of the afterbody base. Axial-force coefficients were obtained for 7^{o} sharp edge and various 15^{o} boattailed afterbodies on which the boattail juncture with the cylindrical portion of the nacelle had been smoothed with different radii of curvature. Data were obtained over a Mach number range of 0.56 to 1.00 at angles of attack from 0^{o} to 8^{o}. The following observations were made:

1. Increasing the value of the radius of curvature to maximum diameter ratio (R/D_M) decreased the drag-rise Mach number of the boattail. With the 15^{o} boattails, the sharp edge ($R/D_M = 0$) configuration had a drag-rise Mach number near 0.6. Increasing

the radius of curvature to $R/D_M = 1$ delayed the drag-rise Mach number to approximately 0.8. For R/D_M of 2.5 or greater, the drag-rise Mach number occurred slightly above Mach 0.9. The 7° sharp-edge boattail also had a drag-rise Mach number near 0.9. At subsonic Mach numbers, increasing R/D_M decreases the boattail axial-force coefficient up to a value of $R/D_M = 3.5$. At Mach 1.0, increasing R/D_M decreases boattail axial-force coefficient over the entire range of R/D_M investigated. The greatest axial-force coefficient reduction obtained was 88 percent at Mach 0.9 for an R/D_M of 3.5. At Mach 0.8, an R/D_M of 0.5 reduced the axial-force coefficient 44 percent, while the same R/D_M at Mach 0.9 resulted in a 27 percent reduction.

2. Increasing the boattail angle of attack beyond 4° caused significant increases in the boattail axial-force coefficient. Angles of attack of 4° or more also resulted in a decrease of the drag-rise Mach number for the 7° conical boattail, but there was no similar effect apparent for the 15° boattails.

3. The presence of the jet simulator reduced the boattail axial-force coefficient for all Mach numbers investigated. For the subsonic Mach numbers, jet simulator data were in agreement with cold jet data interpolated for a value of $p_e/p_o = 1.0$ for 15° boattails with values of R/D_M of 0 and 0.5.

4. Increasing the boundary layer thickness decreased the boattail axial-force coefficient of a 15° conical afterbody with a sharp edge. At Mach 0.9, for example, increasing the boundary layer thickness to model diameter ratio from 0.12 to 0.17 reduced axial-force coefficient about 12 percent.

Lewis Research Center,
National Aeronautics and Space Administration
Cleveland, Ohio, September 8, 1967,
720-03-01-08-22.

REFERENCES

1. Silhan, Frank V.; and Cubbage, James M., Jr.: Drag of Conical and Circular-Arc, Boattail Afterbodies at Mach Numbers from 0.6 to 1.3. NACA RM L56K22, 1957.

2. Felix, A. Richard: Variable Porosity Walls for Transonic Wind Tunnels. Paper presented at the 22nd Semi-Annual Meeting of the Supersonic Tunnel Association, Brussels, Belgium, Sept. 1964.

3. McDonald, H.; and Hughes, P. F.: A Correlation of High Subsonic Afterbody Drag in the Presence of a Propulsive Jet or Support Sting. J. Aircraft, vol. 2, no. 3, May-June 1965, pp. 202-207.

4. Forsgren, L. M.: SST Exhaust Nozzle Boattail Drag Tests at Subsonic and Transonic Conditions. Rep. No. D6-2559, Boeing Compnay, Oct. 1964.

5. Pel, C. and Rustmeyer, A.: Investigation of Turbojet Exhaust-Interference Drag. Rep. No. R-0801-12, United Aircraft Corp. Nov. 1955.

6. Cortright, Edgar M., Jr.; and Kochendorfer, Fred D.: Jet Effects on Flow Over Afterbodies in Supersonic Stream. NACA RM E53H25, 1953.

7. Luidens, Roger W.; and Simon, Paul C.: Aerodynamic Characteristics of NACA RM-10 Missile in 8- by 6-Foot Supersonic Wind Tunnel at Mach Numbers From 1.49 to 1.98. I-Presentation and Analysis of Pressure Measurements (Stabilizing Fins Removed). NACA RM E50D10, 1950.

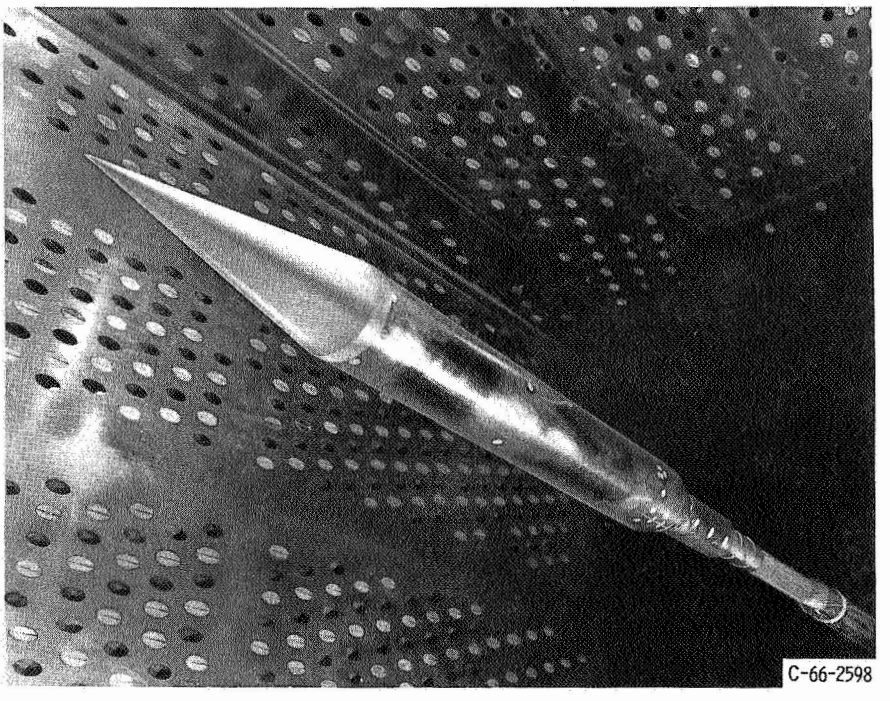

Figure 1. - Afterbody model installed in 8- by 6-foot Supersonic Wind Tunnel.

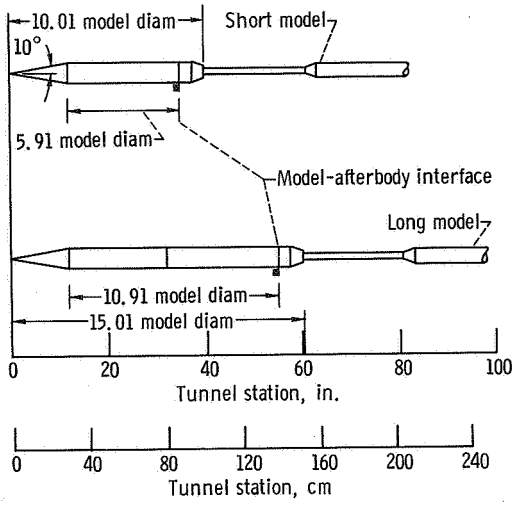

Figure 2. - Model installation showing location of long and short models in 8- by 6-foot perforated test section. Model diameter, 4.00 inches.

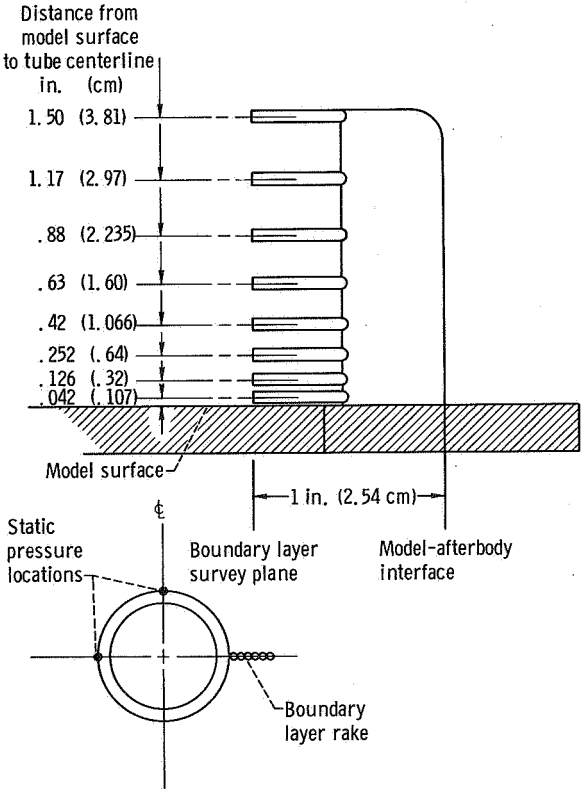

Figure 3. - Boundary layer rake details. (All dimensions are in inches (cm).)

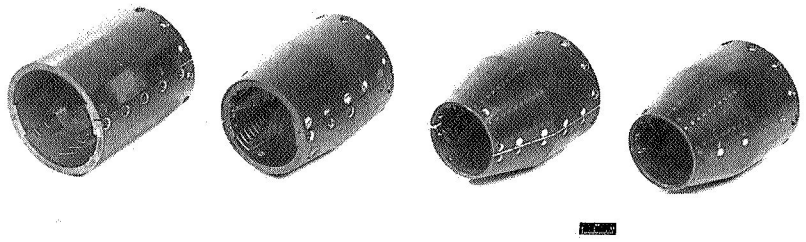

Cylindrical

Boattail trailing-edge angle, 7°; Boattail radius of curvature to maximum diameter ratio, 0.

Boattail trailing-edge angle, 15°; boattail radius of curvature to maximum diameter ratio, 0.

Boattail trailing-edge angle, 15°; boattail radius of curvature to maximum diameter ratio, 0.50.

C-66-4281

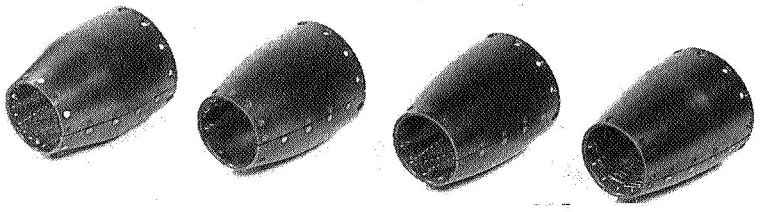

Boattail trailing-edge angle, 15°; boattail radius of curvature to maximum diameter ratio, 1.0.

Boattail trailing-edge angle, 15°; boattail radius of curvature to maximum diameter ratio, 2.50.

Boattail trailing-edge angle, 15°; boattail radius of curvature to maximum diameter ratio, 3.50.

Boattail trailing-edge angle, 15°; boattail radius of curvature to maximum diameter ratio, 4.84.

C-66-4282

Figure 4. - Afterbody geometries investigated.

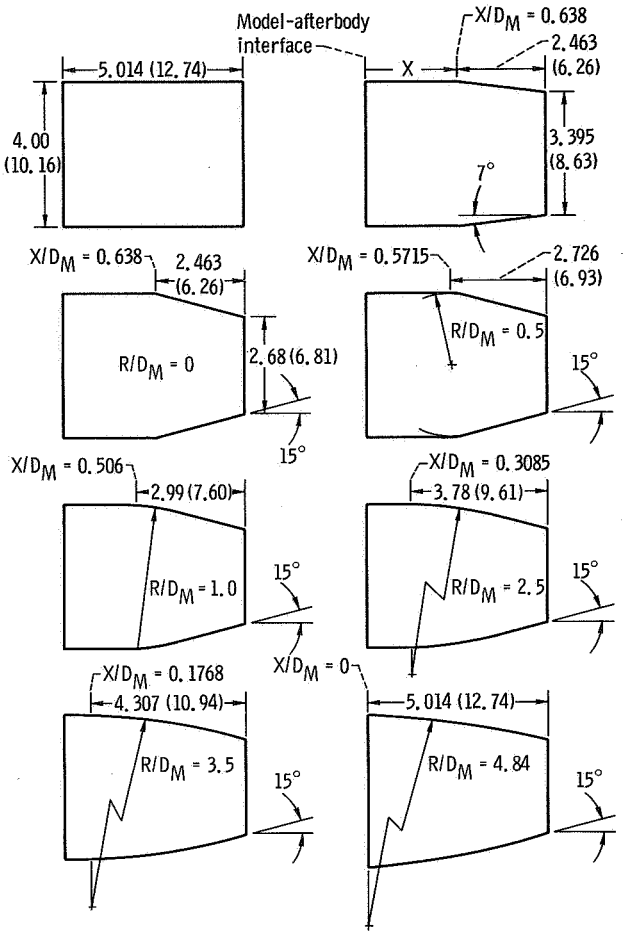

Figure 5. - Afterbody geometry details. (Radius of curvature to maximum diameter ratio, R/D_M; afterbody length to maximum diameter ratio, X/D_M.)

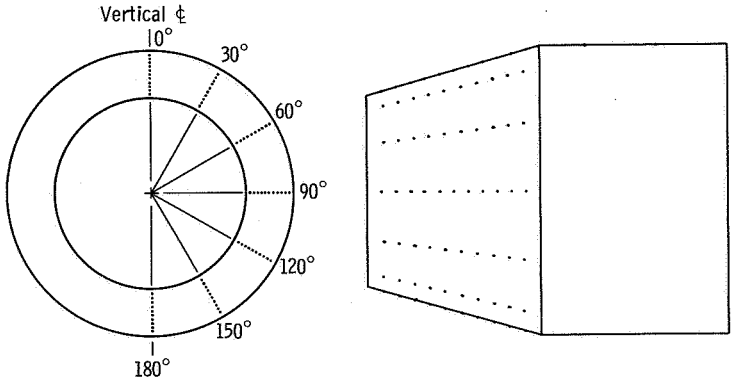

Figure 6. - Afterbody static-pressure instrumentation details.

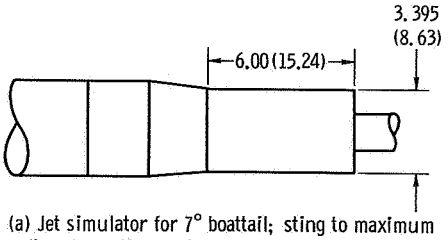

(a) Jet simulator for 7° boattail; sting to maximum diameter ratio, 0.849.

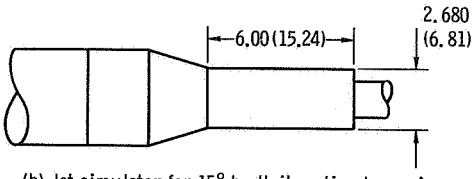

(b) Jet simulator for 15° boattails; sting to maximum diameter ratio, 0.670.

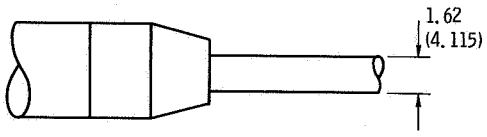

(c) Sting support; sting to maximum diameter ratio, 0.405.

Figure 7. - Base geometry details. (All dimensions are in inches (cm).)

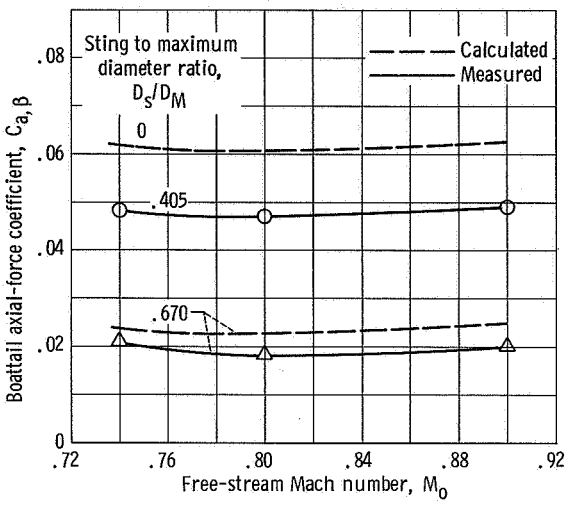

Figure 8. - Effect of sting diameter on boattail axial-force coefficient. Boattail radius of curvature to diameter ratio, 4.84; boattail trailing edge angle, 15°.

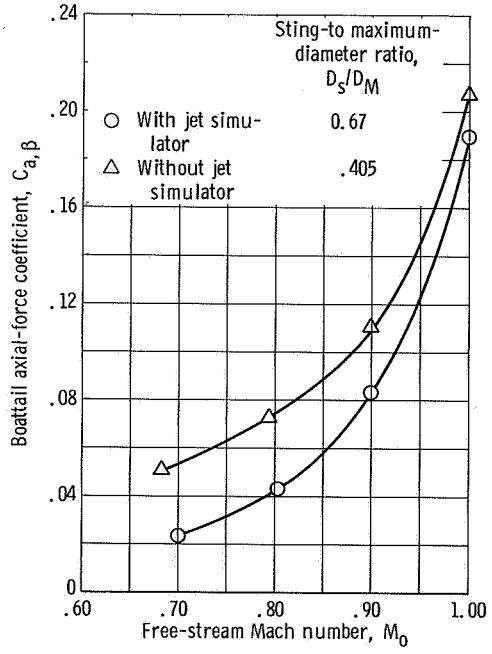

Figure 9. - Boattail axial-force coefficient with and without jet simulator. Boattail radius of curvature to model diameter ratio, 0; boattail trailing-edge angle, 15°; model angle of attack, 0.

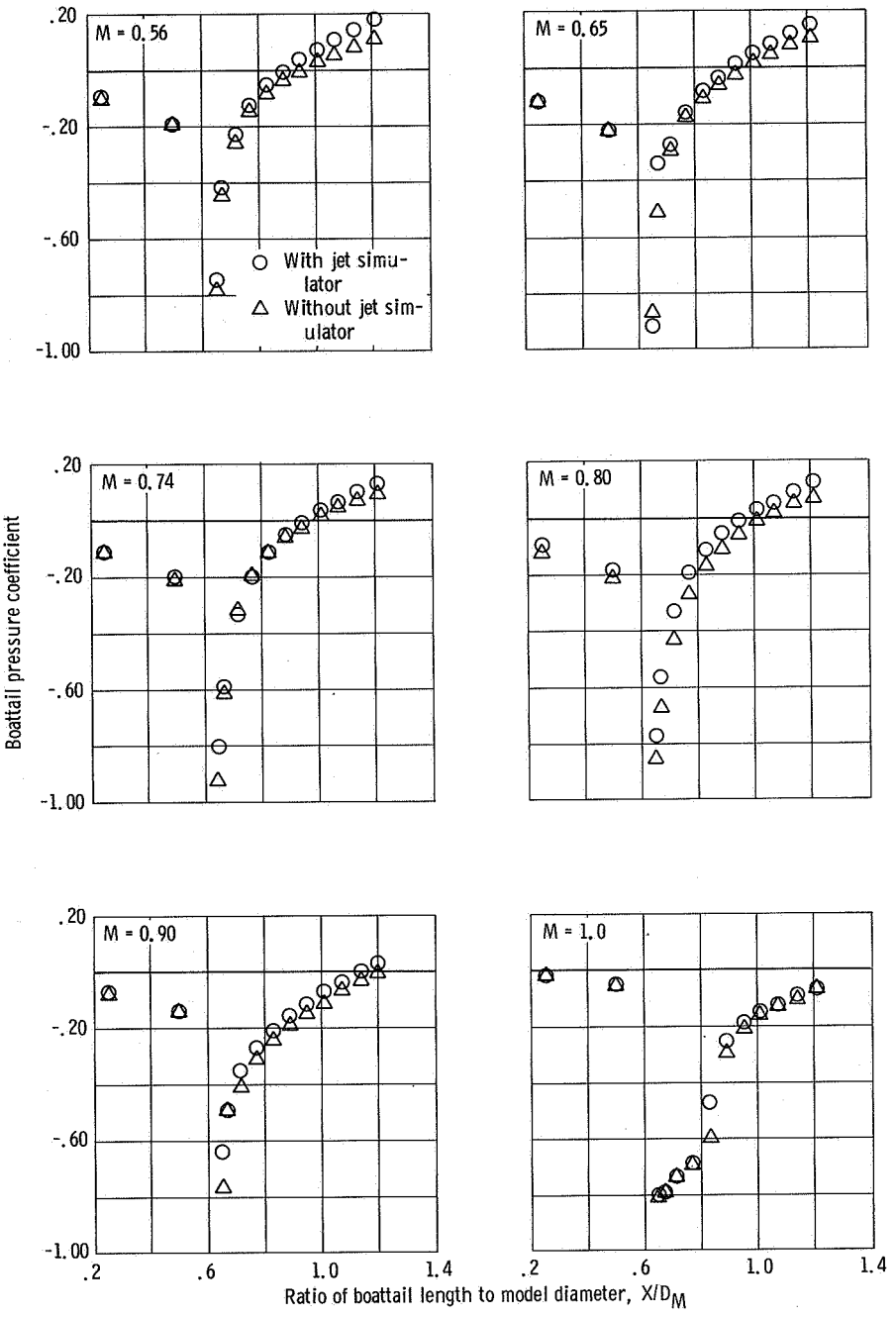

Figure 10. - Effect of jet simulator on boattail pressure distribution. Boattail trailing-edge angle, 15°; boattail radius of curvature to diameter ratio, 0.

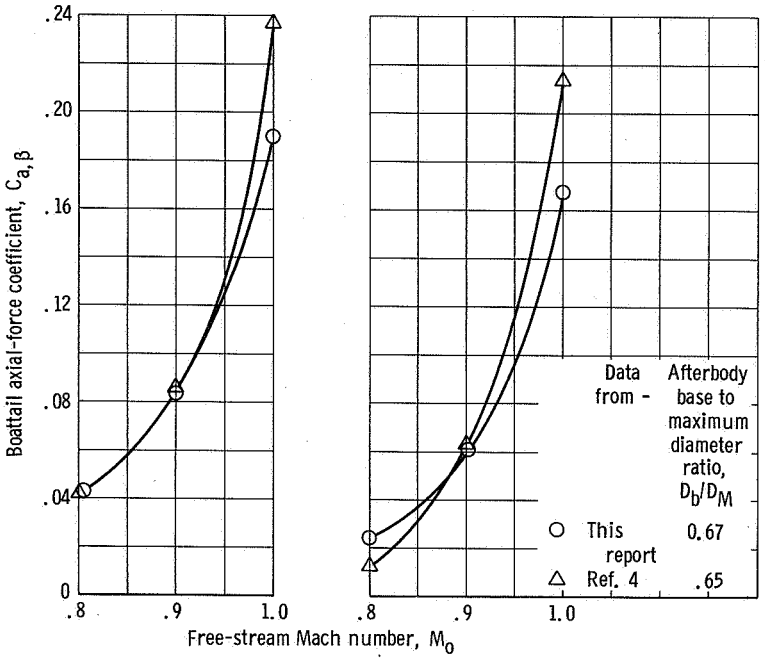

(a) Radius of curvature to maximum diameter ratio, 0.

(b) Radius of curvature to maximum diameter ratio, 0.50.

Figure 11. - Comparison of jet simulator data with cold jet data. Boattail trailing-edge angle, 15°. Reference 4 data is interpolated for static pressure ratio P_e/P_0 of 1.0.

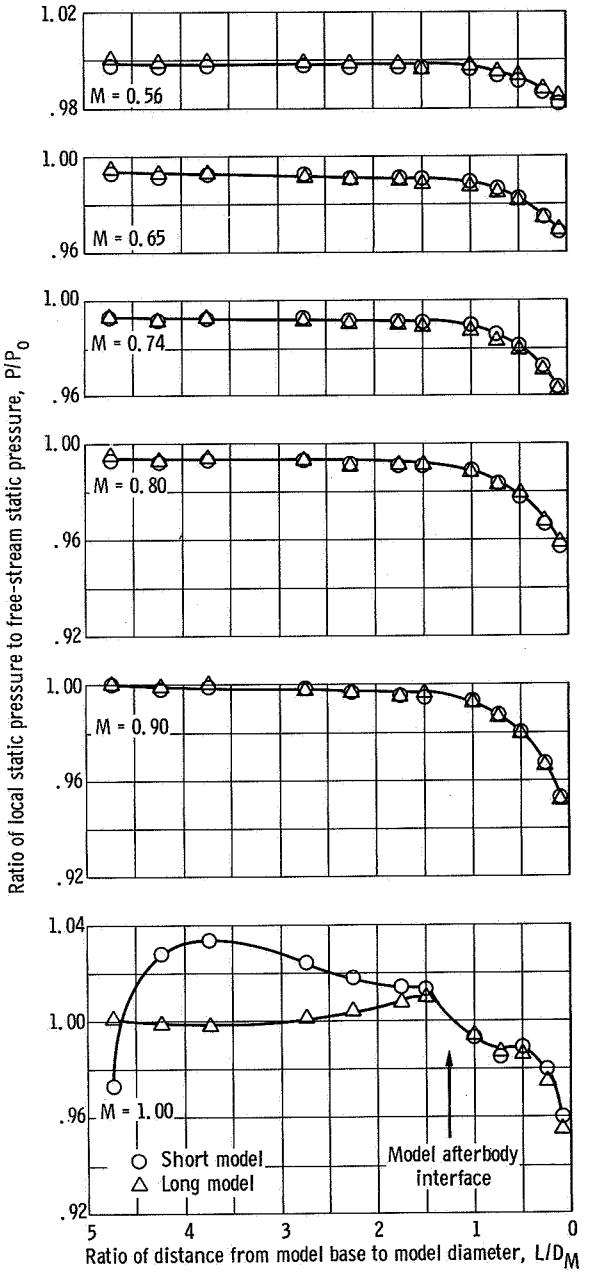

Figure 12. - Pressure distribution on aft portion of model with cylindrical afterbody.

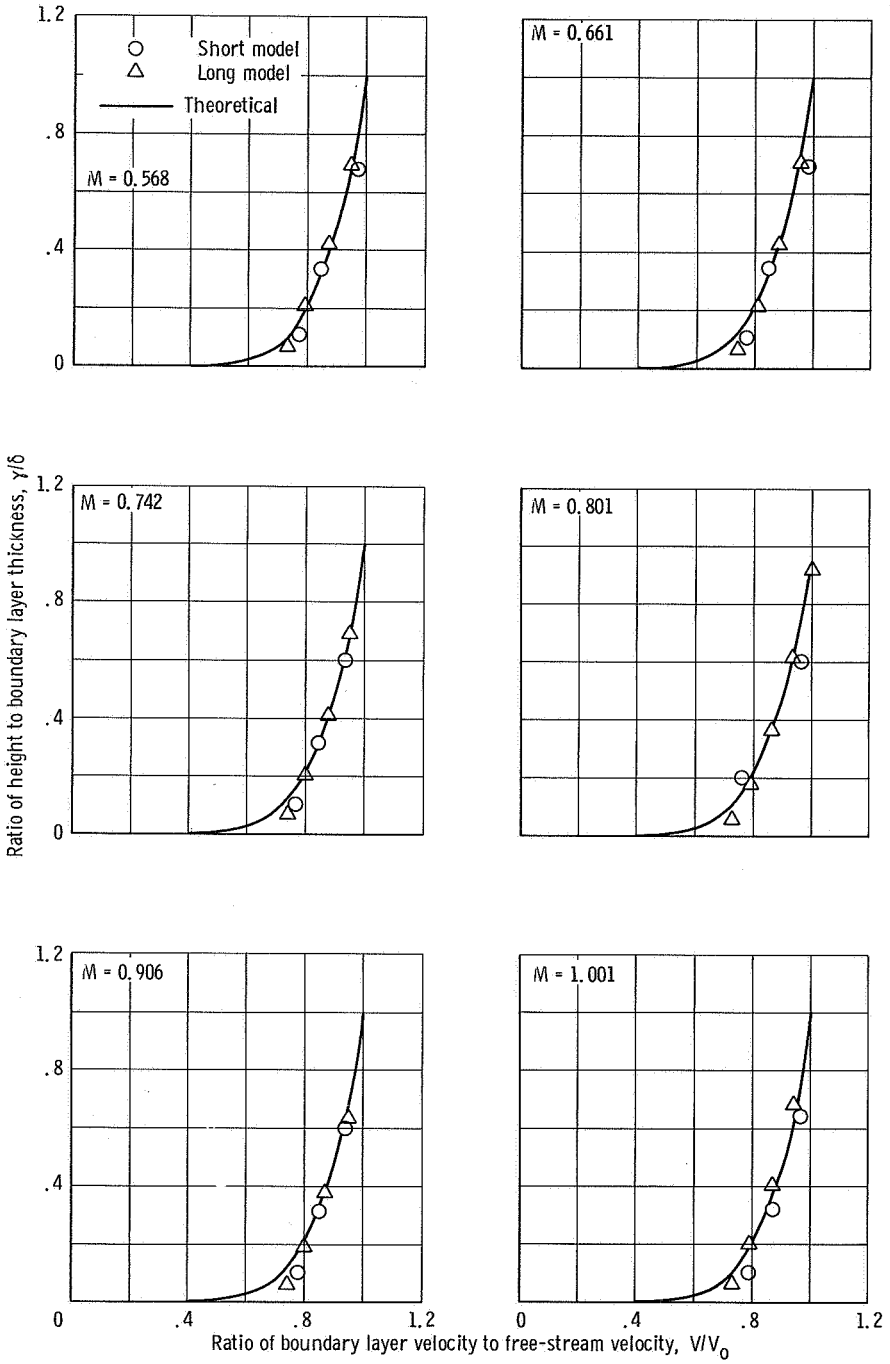

Figure 13. - Boundary layer profiles for short and long models. Comparison of experimental data with theoretical profile for N = 7.

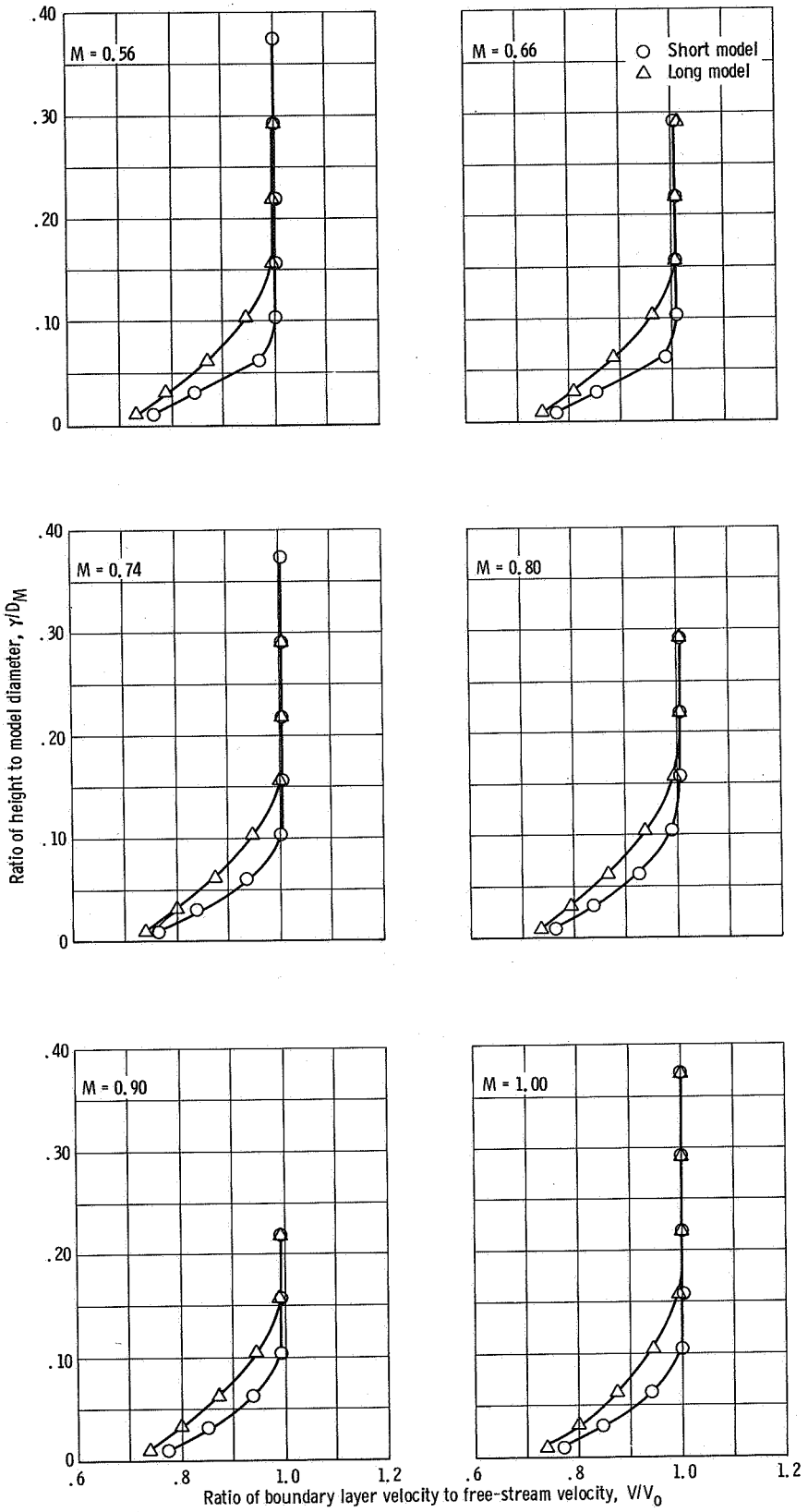

Figure 14. - Boundary layer thickness.

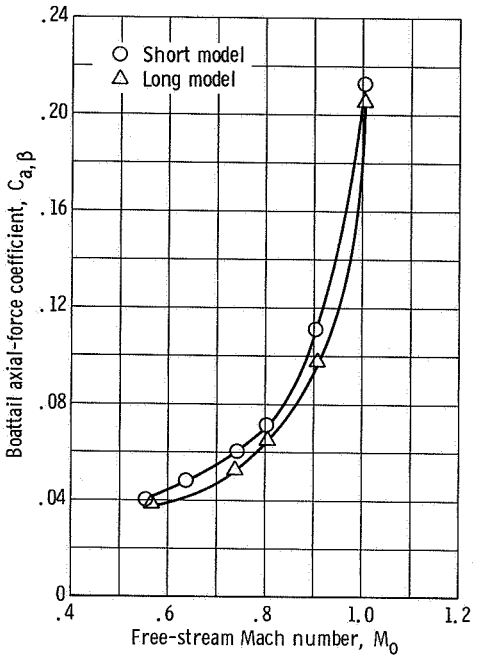

Figure 15. - Boattail axial-force coefficients for short and long models. Boattail trailing-edge angle, 15°; boattail radius of curvature to maximum diameter ratio, 0; diameter of sting, 1.62 inches (4.115 cm); no jet simulator.

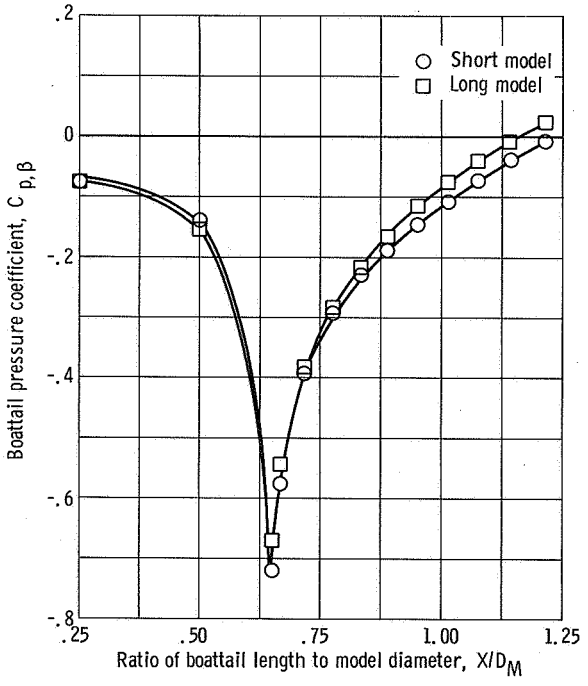

Figure 16. - Effect of boundary layer on boattail pressure distribution. Boattail trailing-edge angle, 15°; radius of curvature to diameter ratio, 0; free-stream Mach number, 0.9.

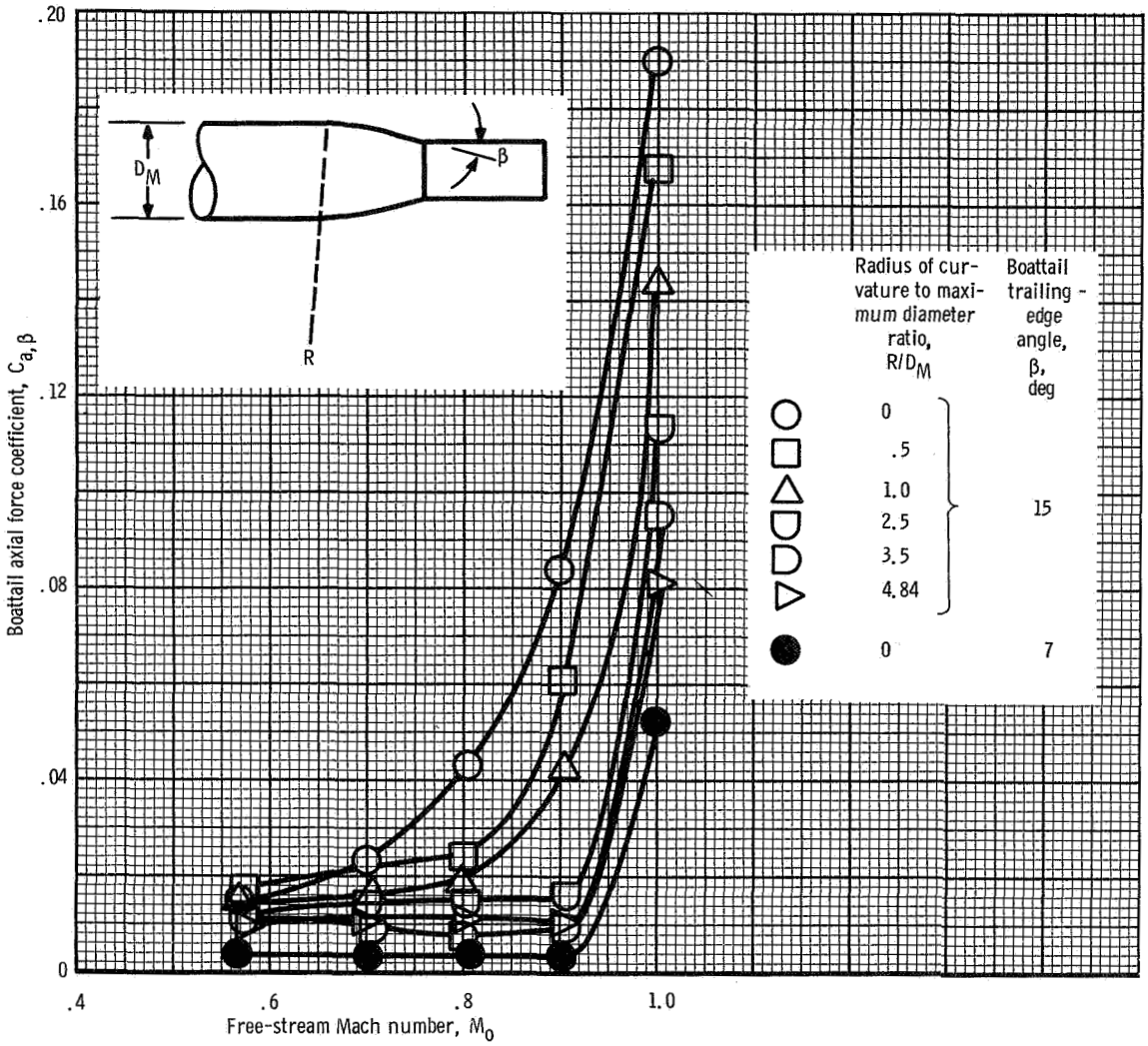

Figure 17. - Effect of afterbody shape on transonic drag rise.

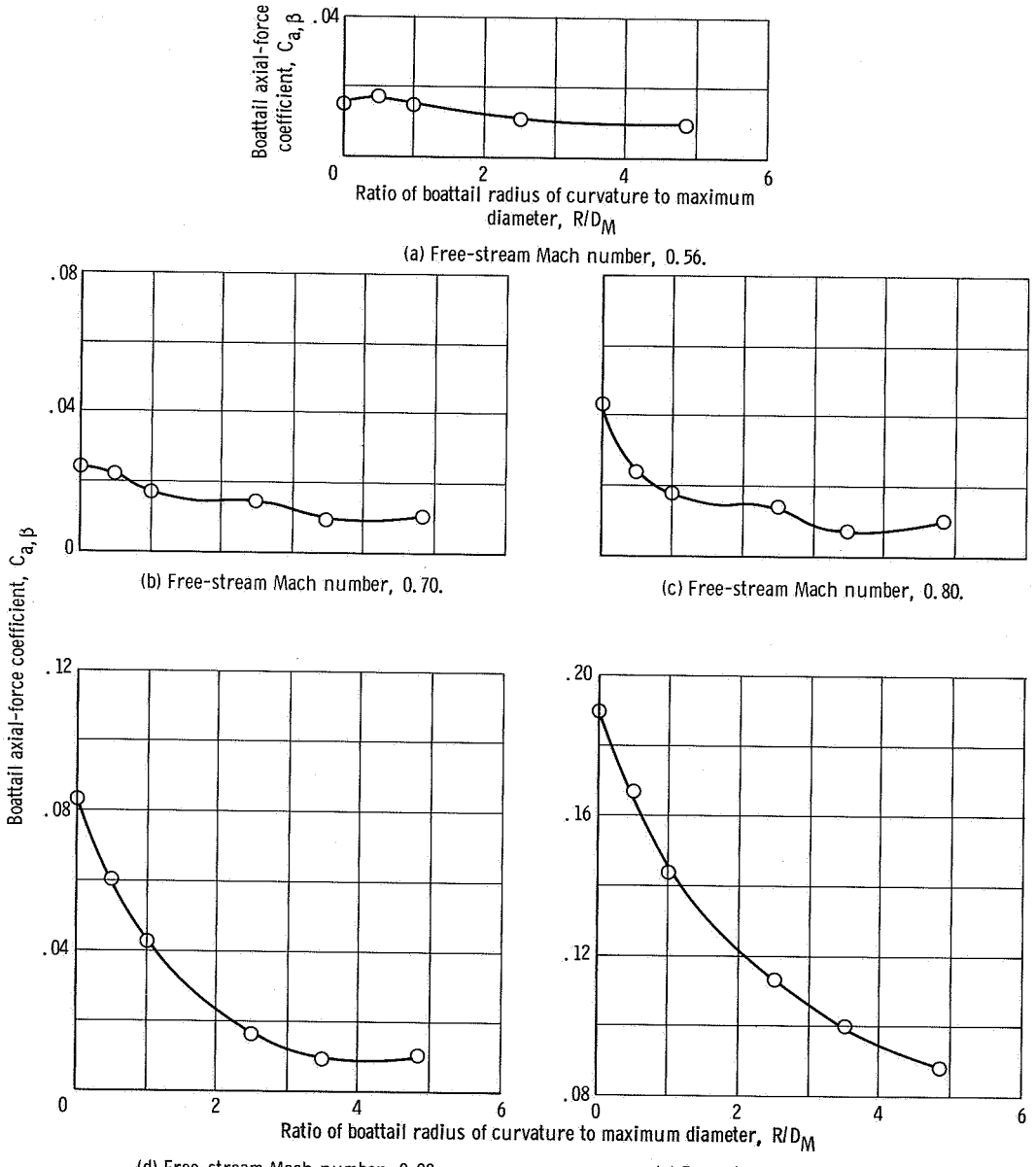

Figure 18. - Effect of radius of curvature to diameter ratio on boattail axial-force coefficient. Boattail trailing-edge angle, 15°; model angle of attack, 0°; with jet simulator.

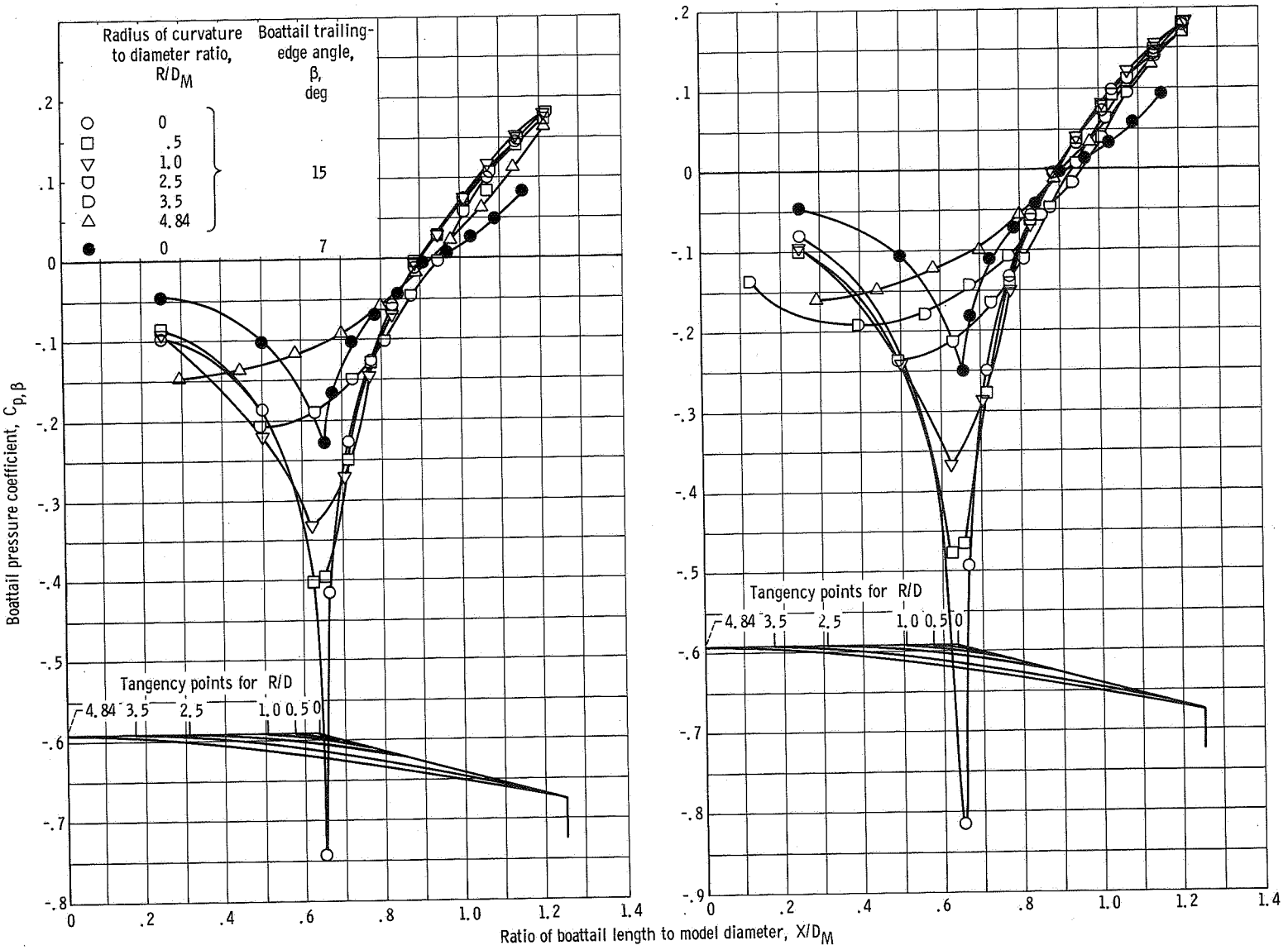

(a) Free-stream Mach number, 0.56.

(b) Free-stream Mach number, 0.7.

Figure 19. - Effect of afterbody shape on pressure distribution.

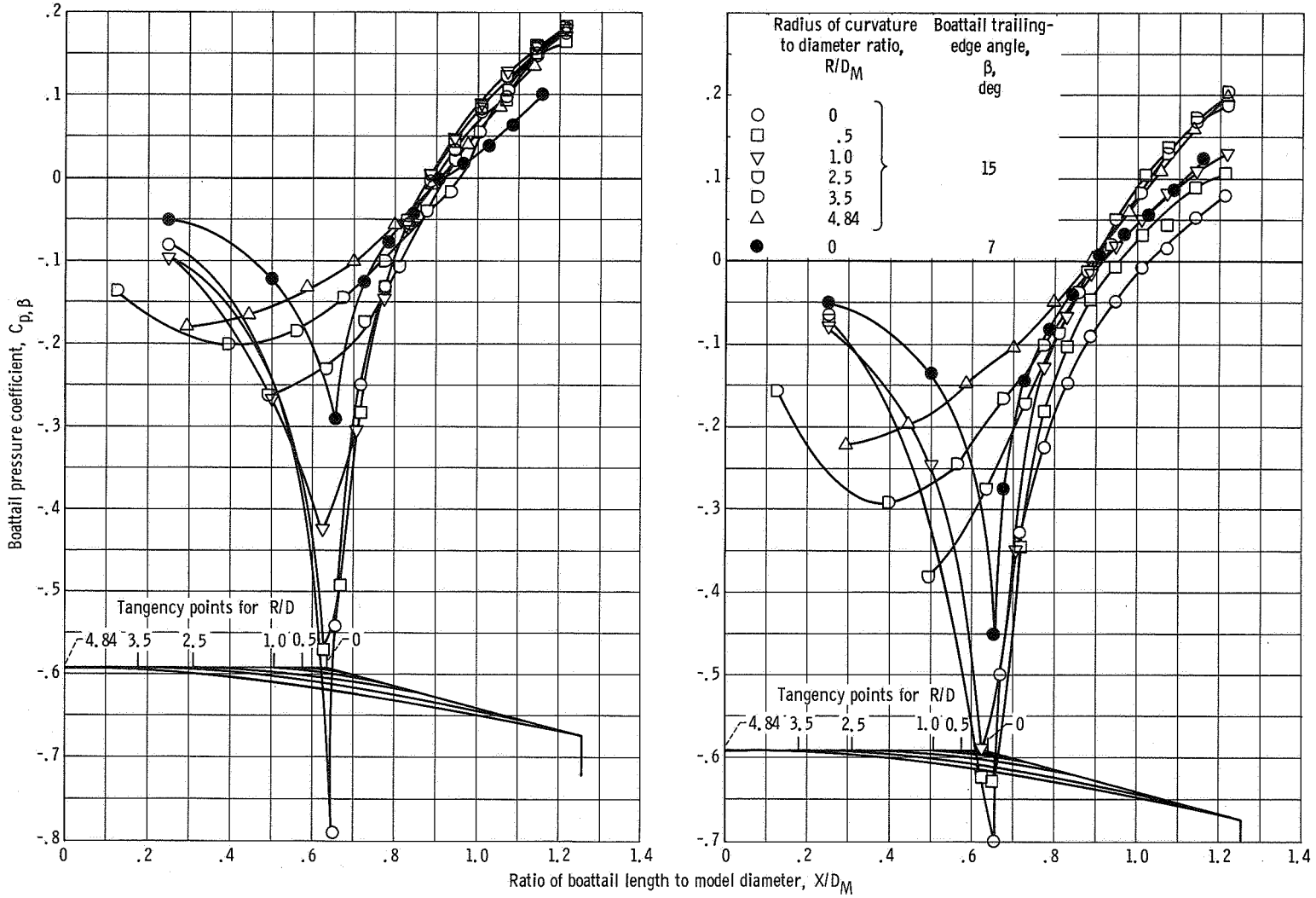

(c) Free-stream Mach number, 0.8.

(d) Free-stream Mach number, 0.9.

Figure 19. Continued.

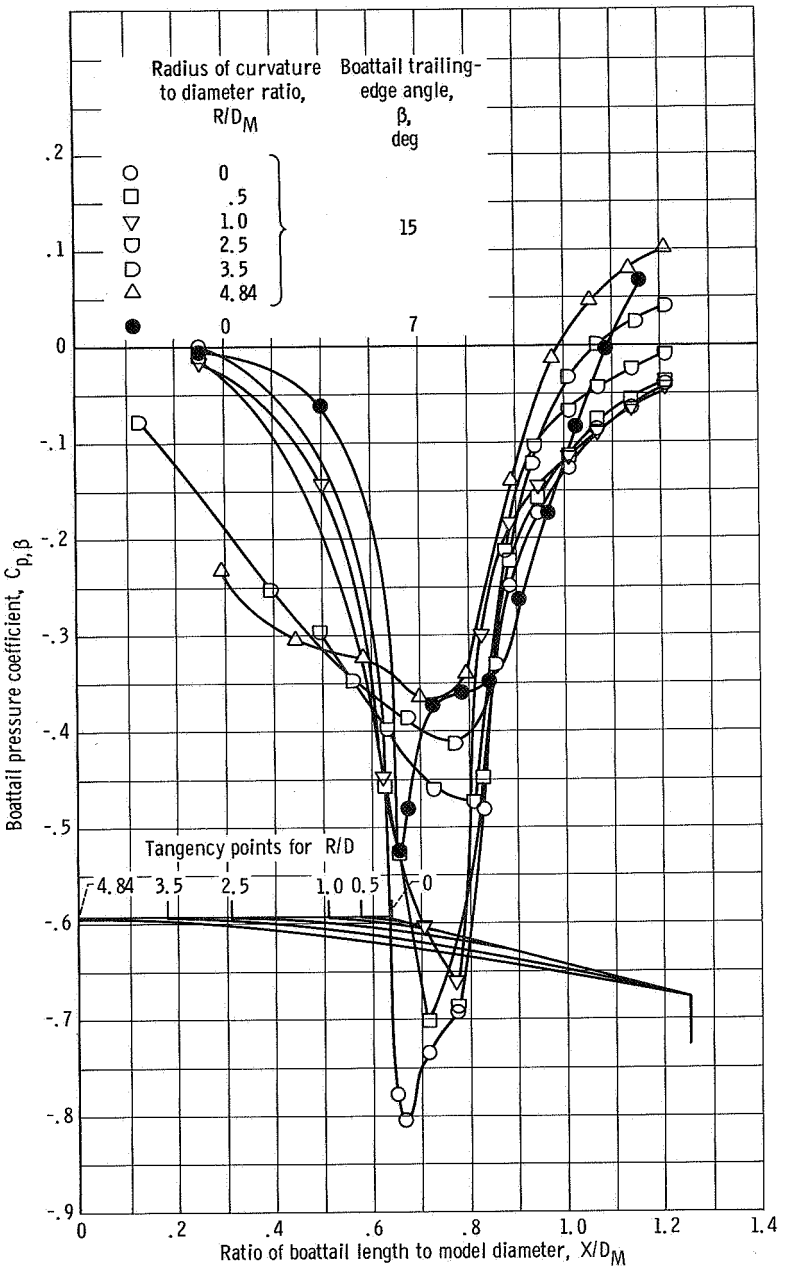

(e) Free-stream Mach number, 1.0.

Figure 19. - Concluded.

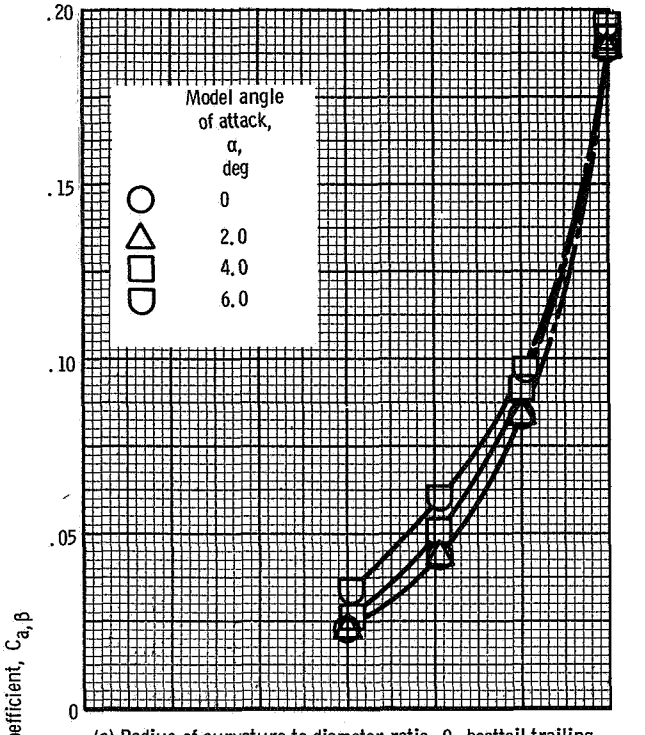

(a) Radius of curvature to diameter ratio, 0; boattail trailing-edge angle, 15°.

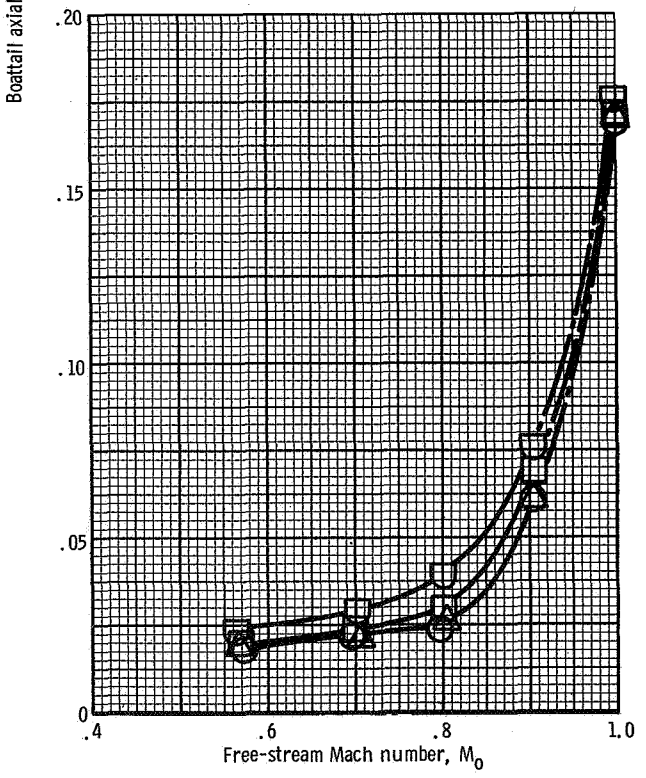

(b) Radius of curvature to diameter ratio, 0.50; boattail trailing-edge angle, 15°.

Figure 20. - Axial-force coefficients at various angles of attack.

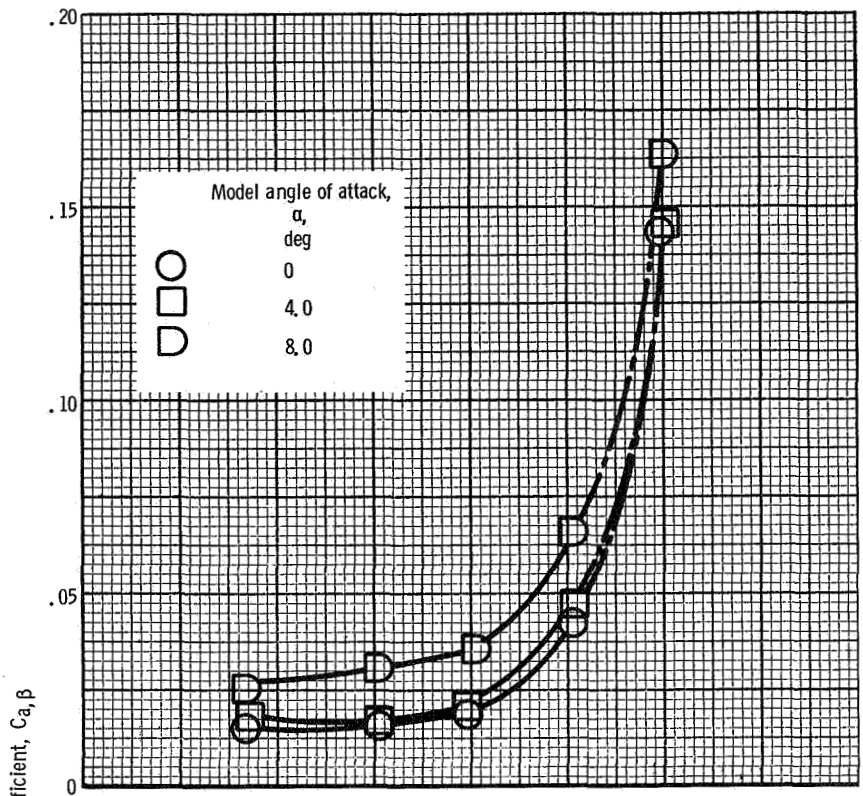

(c) Radius of curvature to diameter ratio, 1.0; boattail trailing-edge angle, 15°.

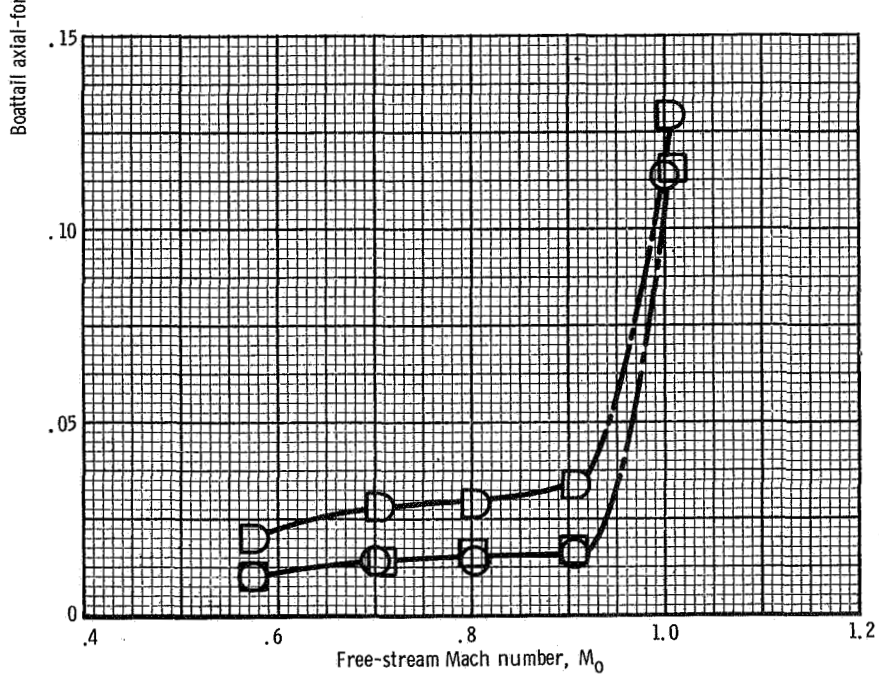

(d) Radius of curvature to diameter ratio, 2.5; boattail trailing-edge angle, 15°.

Figure 20. - Continued.

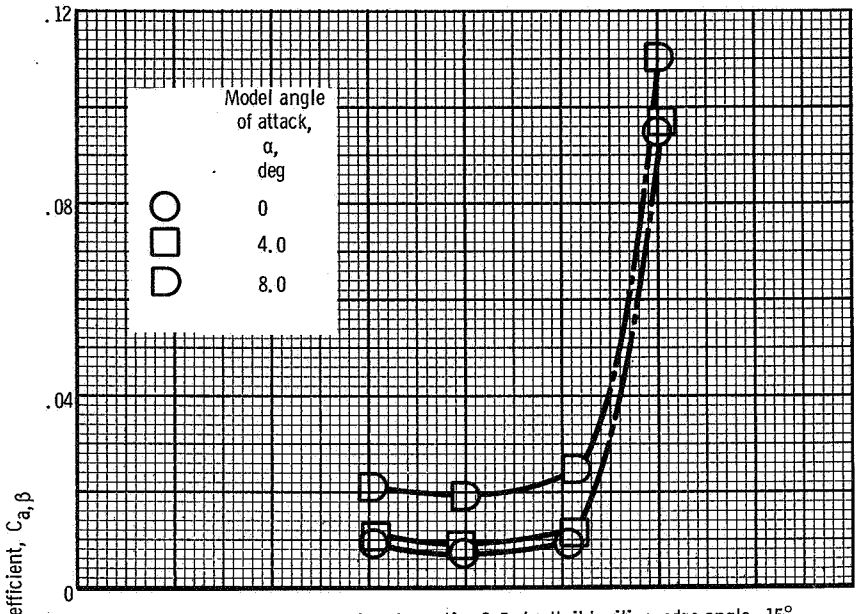

(e) Radius of curvature to diameter ratio, 3.5; boattail trailing-edge angle, 15°.

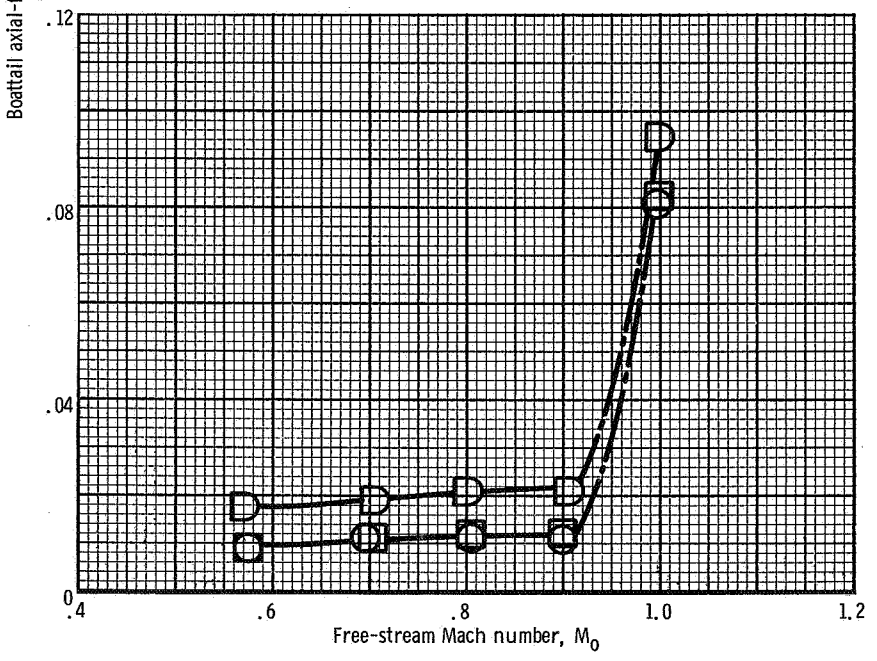

(f) Radius of curvature to diameter ratio, 4.84; boattail trailing-edge angle, 15°.

Figure 20. - Continued.

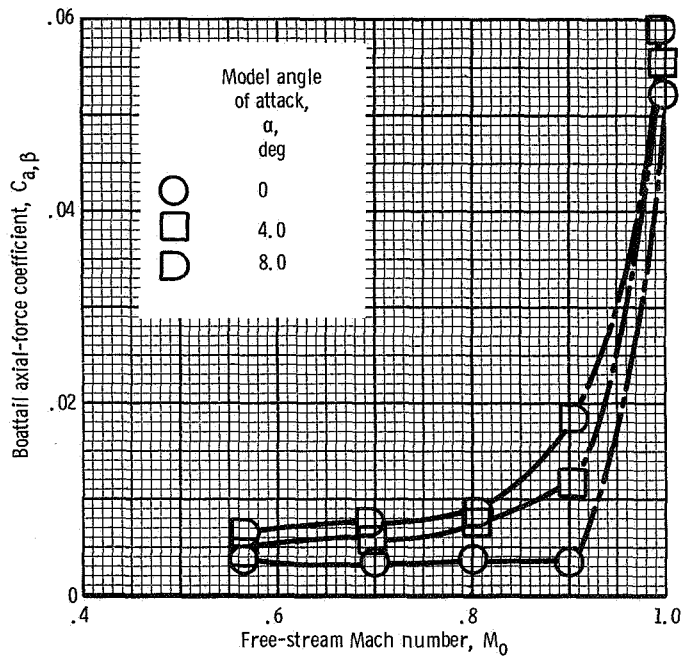

(g) Radius of curvature to diameter ratio, 0; boattail trailing-edge angle, 7°.

Figure 20. - Concluded.

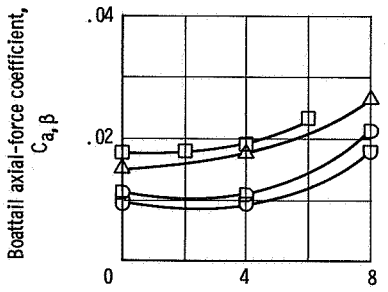

(a) Free-stream Mach number, 0.56.

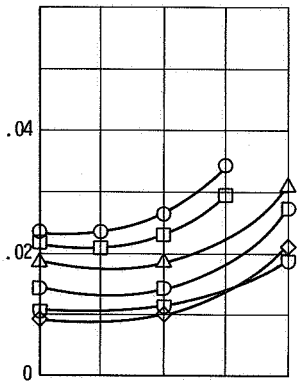

(b) Free-stream Mach number, 0.70.

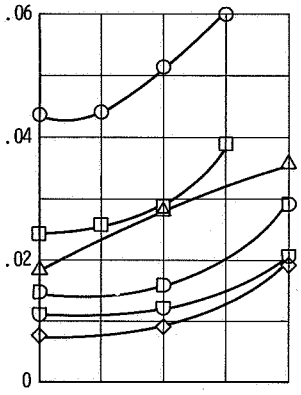

(c) Free-stream Mach number, 0.80.

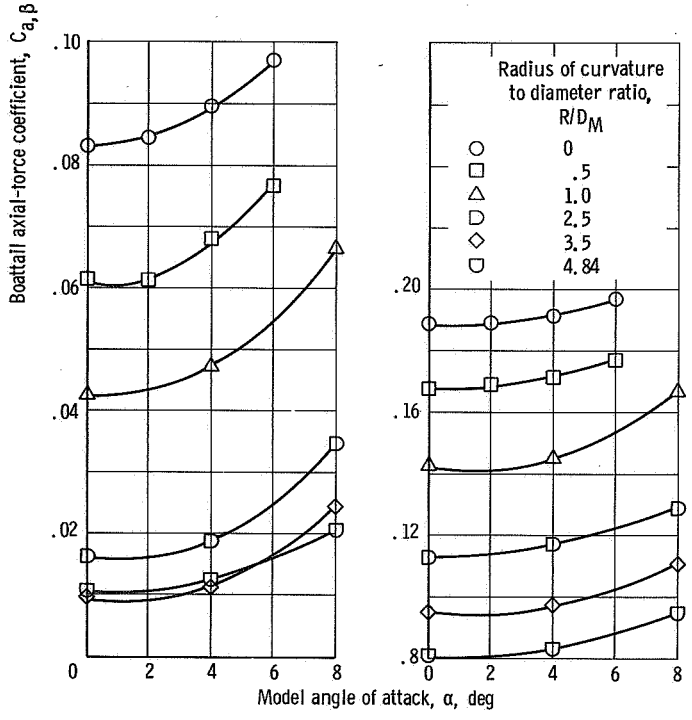

(d) Free-stream Mach number, 0.90.

(e) Free-stream Mach number, 1.00.

Figure 21. - Effect of angle of attack on axial-force coefficient for different boattail radii of curvature; boattail trailing-edge angle, 15°.

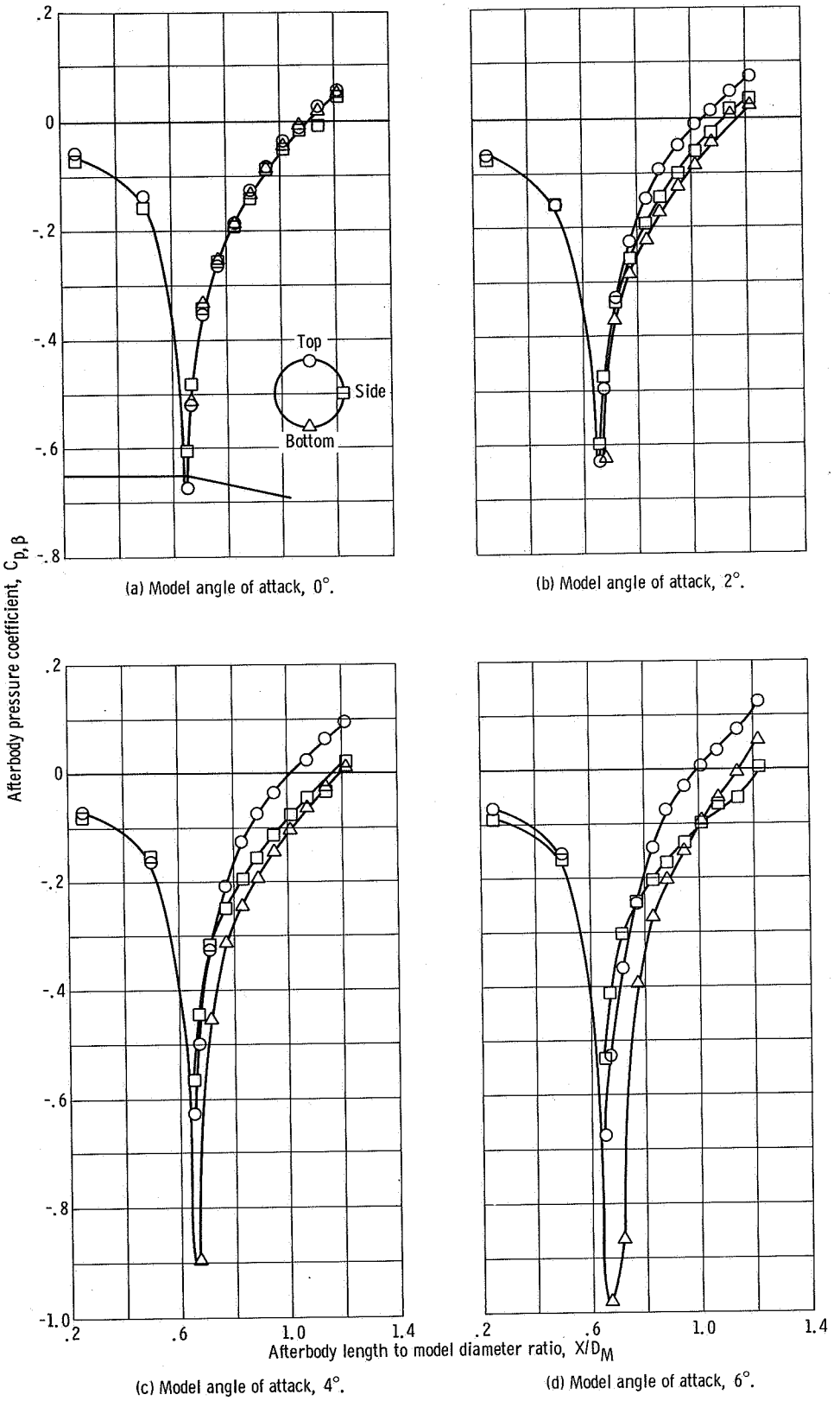

Figure 22. - Effect of angle of attack on pressure distribution. Radius of curvature to diameter ratio, 0; boattail trailing-edge angle, 15°; free-stream Mach number, 0.90.

NASA-Langley, 1968 —— 1 E-3950

"The aeronautical and space activities of the United States shall be conducted so as to contribute . . . to the expansion of human knowledge of phenomena in the atmosphere and space. The Administration shall provide for the widest practicable and appropriate dissemination of information concerning its activities and the results thereof."

—National Aeronautics and Space Act of 1958

NASA SCIENTIFIC AND TECHNICAL PUBLICATIONS

TECHNICAL REPORTS: Scientific and technical information considered important, complete, and a lasting contribution to existing knowledge.

TECHNICAL NOTES: Information less broad in scope but nevertheless of importance as a contribution to existing knowledge.

TECHNICAL MEMORANDUMS: Information receiving limited distribution because of preliminary data, security classification, or other reasons.

CONTRACTOR REPORTS: Scientific and technical information generated under a NASA contract or grant and considered an important contribution to existing knowledge.

TECHNICAL TRANSLATIONS: Information published in a foreign language considered to merit NASA distribution in English.

SPECIAL PUBLICATIONS: Information derived from or of value to NASA activities. Publications include conference proceedings, monographs, data compilations, handbooks, sourcebooks, and special bibliographies.

TECHNOLOGY UTILIZATION PUBLICATIONS: Information on technology used by NASA that may be of particular interest in commercial and other non-aerospace applications. Publications include Tech Briefs, Technology Utilization Reports and Notes, and Technology Surveys.

Details on the availability of these publications may be obtained from:

SCIENTIFIC AND TECHNICAL INFORMATION DIVISION

NATIONAL AERONAUTICS AND SPACE ADMINISTRATION

Washington, D.C. 20546